PCCP

Accepted Manuscript

ROYAL SOCIETY OF CHEMISTRY

www.rsc.org/pccp

Journal Name

RSCPublishing

ARTICLE

Anatase TiO_2 with Nanopores for Dye-sensitized Solar Cells

Cite this: DOI: 10.1039/x0xx00000x

Shuang Yang,[a†] Yi chu Zheng,[a†] Yu Hou,[a] Xiao hua Yang[a] and Hua gui Yang*[ab]

Received 00th January 2012,
Accepted 00th January 2012

DOI: 10.1039/x0xx00000x

www.rsc.org/

In this paper, a serious of mesoporous anatase TiO_2 crystals were prepared through a hydrothermal method. By using different carboxylic acids as solvents and additives, the morphology of the integral crystals as well as inner pores can be tuned by the chain length of the carboxylic acids. Further application of these anatase TiO_2 crystals as the photoanode of DSCs attained an overall energy conversion efficiency of 7.55% because of their low electrical resistive loss and improved light harvesting abilities.

Introduction

Mesoporous titanium dioxide (TiO_2) crystals enabling both desired highly accessible surfaces and long-range orientation of crystal lattice have drawn intensive research attention due to their wide range of applications for such materials: electronics[1-3], optics[4, 5], catalysis[6, 7], energy storage[8-10] and ceramics[11]. The electrical and optical properties of such hierarchical crystals are usually size- and shape-dependent including the inner pores, and, hence, it is essential to be able to control the morphology of the integral crystal as well as inner pores, simultaneously. TiO_2 crystals with a submicrometer-sized diameter, due to their relatively high refractive index and comparable particle sizes to optical wavelengths, are preferred candidates for photon-related applications such as photocatalysis, photonic crystals and dye-sensitized solar cells (DSCs).

As one of the most promising photovoltaic technologies for production of renewable, clean and affordable energy, DSCs have been intensively investigated in recent years.[12-14] For typical efficient DSCs, anatase TiO_2 nanocrystals (≈20 nm) with high surface area is a prerequisite for the TiO_2 layer to ensure the uptake of the dye molecules, thereby yielding large current density and increased photon-to-current conversion efficiency. However, such TiO_2 films normally show high transparency and low light-harvesting ability. One conventional method is to use a light scattering layer of TiO_2 crystals which usually lead to the complication of the device fabrication.[15] As an alternative way towards these problems, submicrometer-sized TiO_2 crystals with nanopores can be used without sacrificing the accessible surface for uptake of dye molecules. Therefore, it is of extremely importance to regulate not only the morphology of the integral crystals which governing the light-scatting property, but also the pore structures which ensures the dye loading amount and electrolyte diffusion. Moreover, the crystal defects and grain boundaries must be minimized to reduce the loss during electron transport by charge recombination or back reaction.[16] However, it is still a great challenge to regulate the whole morphology of the mesoporous crystals as well as the internal pore structures. It has been known that the capping agents or solvents are usually employed in the controllable synthesis of crystals and may further provide opportunities for controlling synthesis of crystals with nanopores.[17]

Herein, we developed a simple synthetic strategy to produce a series of mesoporous anatase TiO_2 crystals. Carboxylic acids were employed as solvents and additives to synthesize TiO_2 crystals with nanopores. The integral shapes, pore structures and the nanosized subunits can also be controlled by the molecular structures of the carboxylic acids. It is noteworthy that the crystal lattices of the subunits have the similar orientation leading to a single-crystal-like structure with reduced defects of grain boundaries significantly. Consequently, by the rational selection of mesoporous crystals, the light-scattering ability, dye molecule loading amount, electron transport property and electrolyte diffusion can be optimized. We applied these anatase TiO_2 single layer films with a thickness of 12 μm as photoanode of DSCs and attained an overall energy conversion efficiency of 7.55%.

Experimental

Synthesis of Mesoporous Anatase TiO_2

The mesoporous anatase TiO_2 was synthesized by a modified hydrothermal reaction of titanium precursor and carboxylic acids.[18] Typically, 0.5 mL Titanium (IV) isopropoxide (TTIP) was added dropwise to 20 mL of formic acid, acetic acid, octoic acid or oleic acid under stirring,

respectively. The obtained white suspension was transferred to a 50 mL Teflon-lined stainless-steel autoclave, which was then heated at 200 °C for 24 h. After the autoclave cooled to room temperature, the product was collected by centrifugation, washed with deionized water and ethanol several times.

Fabrication of DSCs

The FTO glass was first cleaned in a detergent solution using an ultrasonic bath for 15 min and rinsed with water and ethanol twice. Then the FTO glass plates were immersed into a 40 mM aqueous $TiCl_4$ solution at 70 °C for 30 min and washed with water and ethanol. For the preparation of nanoporous TiO_2 layer, the viscous pastes were prepared according to the literature.[15] A 12 μm thick layer of the as-prepared TiO_2 particles was loaded on the fluorine doped SnO_2 (FTO) conducting glass (NSG, 8 Ω/square) by screen printing technique followed by sintering at 500 °C. After cooling to 80 °C, the two layers of TiO_2 films were immersed in a 5×10^{-4} M solution of N719 dye (Solaronix SA, Switzerland) in acetonitrile/tert-butyl alcohol (V/V=1/1) for 24 h. The Pt-electrode was prepared by drop-casting 0.5 mM H_2PtCl_6/ethanol solution on the clean FTO conductive glass. Subsequently, the FTO glass coated with Pt was then sintered in a muffle furnace at 450 °C for 30 min.

Characterization

The morphology and structure of the samples were characterized by high-resolution transmission electron microscopy (HRTEM, JEOL JEM-2010F, F20, 200 kV), field emission scanning electron microscopy (FESEM, HITACHI S4800) and X-ray diffraction (XRD, Bruker D8 Advanced Diffractometer, Cu Kα radiation, 40 kV). The current-voltage tests of DSCs were performed under one sun condition using a solar light simulator (Oriel, 91160, AM 1.5 globe). The power of the simulated light was calibrated to 100 $mW\cdot cm^{-2}$ using a Newport Oriel PV reference cell system (model 91150 V). The EIS experiments were measured in the dark using an electrochemical workstation (Parstat 2273, Princeton). The frequency range of EIS experiments was from 100 kHz to 100 mHz with an AC modulation signal of 10 mV and bias DC voltage of 0.60 V. The curves were fitted by the Zview software. The amount of adsorbed dye was measured by desorbing the dye into 10 mM NaOH solution and measuring the absorption peak intensity of N719 at 515 nm with a Cary 500 Spectrophotometer. The diffuse-reflectance spectra were measured by using a Cary 500 Spectrophotometer.

Results and discussion

Mesoporous anatase TiO_2 crystals were prepared by a simple hydrothermal method using carboxylic acids with different chain length as solvents and surfactants. When formic acid (HCOOH) was used, highly monodispersed octahedral TiO_2 (H1) was formed in. The scanning electron microscopy (SEM) image in Figure 1 (a, b) shows the as-prepared H1 sample

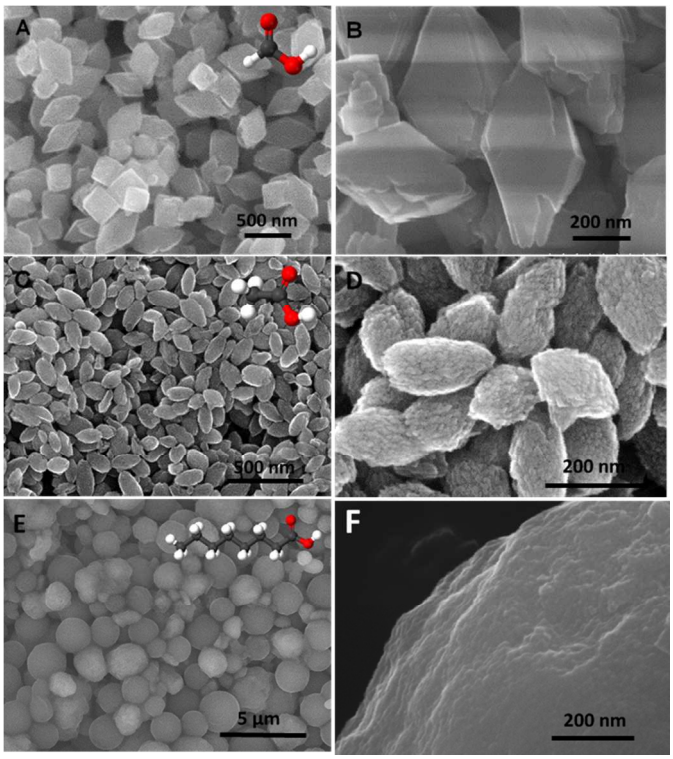

Figure 1. SEM images of (A, B) H1; (C, D) H2; (E, F) H3. The insets in (A, C and E) are the corresponding 3D molecular structures of the solvents.

with a whole size of about 400 nm composed of small particles about 50 nm and a relative smooth surface with few pores. Then, in acetic (CH_3COOH), we found a spindle shaped structure (H2) was generated and the crystal size was reduced to about 150 nm (Figure 1C). As illustrated by the high-magnification SEM image (Figure 1D), nanosized subunits (14-18 nm) and pores (≈8.6 nm) could be observed on the comparatively rough surface of these mesoporous TiO_2 crystals. Moreover, the geometry of the TiO_2 crystals (H3) synthesized in octoic acid ($C_7H_{15}COOH$) varied from polyhedrons with two sharp ends to well-defined micrometer scale spheres as shown in Figure 1E. Interesting, the size of the subunits was further reduced to about 10 nm as presented in Figure 1F. The smaller size may be as a result of the intense interaction between the titanium species and capping agents which retard the hydrolysis process. Concerning the effect of the chain length of carboxylic acids, a further increase of oleic acid ($C_{17}H_{33}COOH$) is also resulted in micrometer scale spheres as shown in Figure S2.

Figure S1 shows the typical XRD pattern of the sample H1, H2 and H3, the diffraction peaks with $2\theta=25.3^o$, 37.8^o and 48.1^o can be indexed to (101), (004), and (200) crystal planes of anatase TiO_2 (tetragonal,I41/*amd*, JCPDS 21-1272), respectively, confirming their pure anatase TiO_2 phase. Compared with H3, The diffraction peaks for samples H1 and H2 are sharper and the (103) and (112) reflections were better resolved, but those of the H3 sample were congested and unresolved; this condition suggests the long chain solvents may retard the course of crystallization.

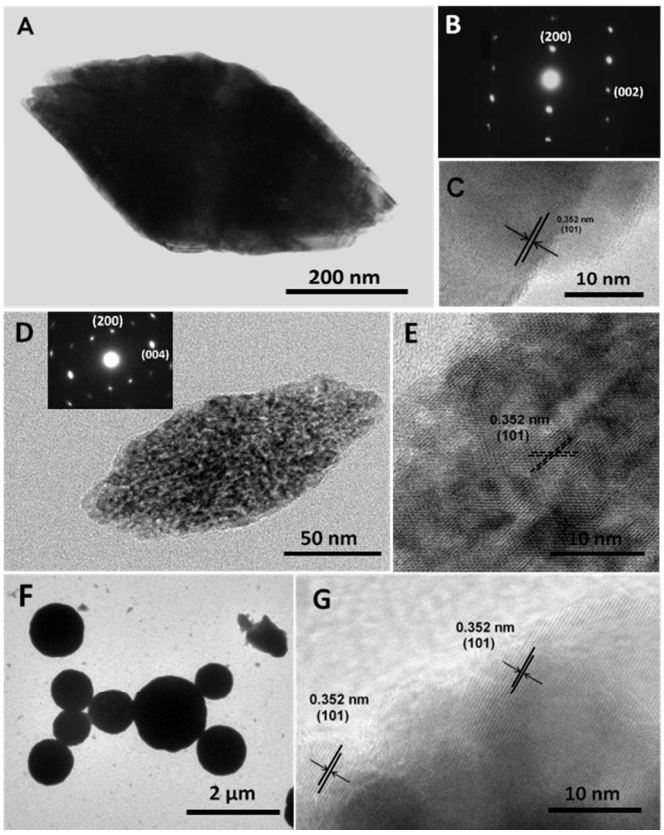

Figure 2. Typical TEM and HRTEM images of (A, C) H1; (D, E) H2; (F, G) H3. (B) and the inset in (D) are the related SAED pattern of H1 and H2, respectively.

The detailed morphology of the mesoporous nanocrystals was monitored via transmission electron microscopy (TEM)and high-resolution TEM (HR-TEM) in Figure 2. The typical TEM images (Figure 2A and 2D) again confirmed that the integral particles of H1 and H2 are composed of nanosized subunits. The related selected area electron diffraction (SAED) patterns (Figure 2B and the inset in Figure 2D) display slightly elongated diffraction spots corresponding to the [002] zone of the anatase phase, indicating that the whole particle has a single-crystal-like structure. It is known the clear diffusion spots generally indicate low defect level of single crystals, and the electron diffusion patterns present here is small diffusion spots clearly which suggest the reduced defects and high orientations of theses crystals. Lattice images of H1 and H2 were clearly observed (Figure 2(C, E)), illustrating assemble of the nanoparticle subunits is highly oriented along [001] direction. Although the sample H3 has a sphere shape (Figure 2F), interestingly, we also found that the lattice of subunits was aligned at some orientation as shown in the HRTEM image of Figure 2G. Noteworthy, when $C_{17}H_{33}COOH$ was used as the solvent, crystal lattices staggered together without any obvious orientation among the subunits after the assemble process (Figure S3). Therefore, the long carbon chain may impede the solute diffusion which further leads to the disordered arrangement of the crystal subunits.

Combining these results, we can reasonably conclude that the chain length of carboxylic acids plays the pivotal role in the nucleation, growth and assemble process of the crystals which further governs the crystal size, shape, pore structure and even crystallinity. We presume that the steric effect and high viscosity of long chain acids would hinder the diffusion of the solute, stabilize the Ti species and reduce the extent of orientation during the crystal assembling process. Therefore, the subunits of fromic acid has a regular octahedron shape with relative large crystal size. This further leads to the complete assembling into single-crystal-like octahedrons. With the increase in chain length of carboxylic acids, the geometry of crystals evolved from octahedrons to spindles and finally spheres together with the reduction of subunit size and crystallinity.

Brunauer-Emmett-Teller (BET) specific surface area (S_{BET}) measurement was performed to further reveal the pore structures including specific surface area, porosity, and surface roughness factor of the mesoporous crystals (Figure 3). Type IV isotherms with H1 type hysteresis loops were observed, which have a sharp capillary condensation step in the relative pressures of 0.8-0.95 for H1 and H2, 0.5–0.9 for H3, indicating their well homogeneity of the samples and relatively small pore sizes. From the specific surface areas shown in Table 1, a similar tendency can be found in consistent with TEM results. In the case of H1 sample, the specific surface area is only 7.99 m^2/g and there is only a weak peak centered at 2.5 nm shown in the corresponding pore size distribution curve, suggesting the dense octahedral structure with bits of pores. With the increase of chain length of carboxylic acids, the specific surface areas of H2 and H3 rise to 133.12 and 77.62 m^2/g because the long chain acids can support and produce larger pores efficiently.

Sample H1-H3 and Degussa P25 were applied as the nanoporous TiO_2 electrodes of DSCs with identical components—N719 dye, iodide/triiodide electrolyte, and Pt counter electrodes. All samples were subjected to measurements of current–voltage (*J–V*) characteristics under

Table 1. Comparison of BET surface areas, short-circuit photocurrent density (J_{sc}), open-circuit photovoltage (V_{oc}), fill factor (*FF*), overall light-to-electricity conversion efficiency (η) along with the amount of adsorbed dye N719 for the photoanodes made of P25, H1, H2 and H3, respectively.[a]

DSC Samples	S_{BET} Value [m^2/g]	Dye loading [10^{-7} mol/cm^2]	J_{sc} [mA·cm^{-2}]	V_{oc} [mV]	*FF* [%]	η [%]
P25	50±15	1.18	13.0	785	0.60	6.11
H1	7.99	0.64	6.5	760	0.68	3.37
H2	133.12	1.69	14.7	810	0.64	7.55
H3	77.62	1.56	13.1	800	0.66	6.92

[a] The active areas of the photoelectrodes were about 0.25 cm^2 with similar film thickness.

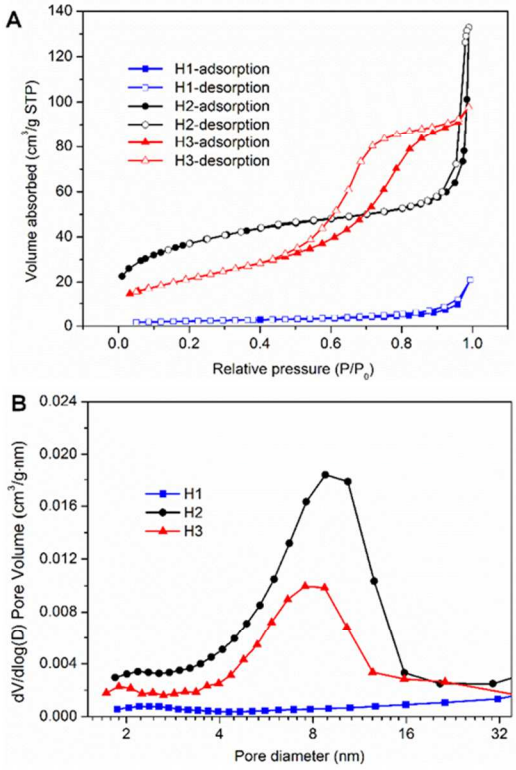

Figure 3. BET results of the sample H1, H2 and H3 adsorption–desorption isotherms (a) and pore size distribution curves (b) from Barrett–Joyner–Halenda (BJH) method.

illumination of AM1.5 simulated sunlight with a power density of 100 mW cm^{-2} (Figure 4A) and the photovoltaic characteristics obtained are summarized in Table 1. With relatively small J_{sc} (7.99 mA·cm^{-2}) and V_{oc} (760 mV), the cell based on sample H1 presented an energy conversion efficiency (η) of 3.37%. This small J_{sc} is in registry with the low pore volume of sample H1 which showed inadequate uptake of dye molecule. Compared with P25 photoanode, sample H2 and H3 presents higher J_{sc} due to the enhancement of dye loading amounts. The performance of H2 photoanode was further improved with a J_{sc} of 14.7 mA·cm^{-2}, a V_{oc} of 810 mV and an *FF* of 0.64 reaching a η of 7.55%. In the nanoporous films, electron diffusion is determined by trapping/detrapping events along the sites of the electron traps (defects, surface states, grain boundaries, self-trapping etc.) that generally at TiO_2 surface and of significant importance at the interface between TiO_2 nanoparticles.[2, 19] The electron transfer in the P25 film may be limited by the recombination of the weak connection or crystal defects between the grain boundaries which result in low J_{sc} values. The higher V_{oc} of H2 sample can be explained as a consequence of reduced charge recombination because of the reduced surface defects derived from the inner single-crystal-like structure, leading to an increase of electron density, and thus the shift of the Fermi level.[20] As discussed above, we expect that the single-crystal-like mesoporous TiO_2 crystals could avoid the high defect levels of the necking particles and provide path ways for electrons transfer directly.

Typical photoanodes constructed of TiO_2 nanoparticles usually show transparency and have negligible light-scatting properties, indicating the transmission of large fraction of the visible light. This phenomenon can be explained by the Rayleigh scattering theory with the following equation:

$$I = I_0 \frac{\mathrm{I} + \cos^2\theta}{2d^2}\left(\frac{2\pi}{\lambda}\right)^4 \left|\frac{m^2-1}{m^2+2}\right|^2 r^6 \qquad (1)$$

where I_0 is the incident intensity, d is the distance to the particle, and y is the scattering angle. From the equation, Rayleigh scattering intensity is proportional to the 6th power of particle size and thus, light scatting centers with large size are desired for promoting light- quantified by diffuse reflectance spectroscopy as shown in Figure 4D. All films represent high diffuse reflection in the ranges from 380 to 450 nm, but a distinctly rapid decline in light-scattering capability is observed for P25 film in the wavelength range from 500 to 800 nm. The H2 and H3 film, by contrast, have better light scattering properties in the visible and particularly in near-infrared regions, implying that the incident light was significantly scattered within the film of mesoporous TiO_2 crystals due to the comparable crystal size to the wavelength of visible light.

To confirm the above inferences, electrochemical impedance spectra (EIS) was employed to explore the electron transport property of DSCs based on H1, H2 and H3 photoanodes as depicted in Figure 4C. An equivalent circuit (the inset in Figure 4C) was given to fit the series resistance (R_s), charge-transfer resistance (R_1, R_2, and W_s) and the corresponding constant phase angle element (CPE) in DSCs. [21-25] It is generally accepted that the series resistance (R_s) is mainly related to

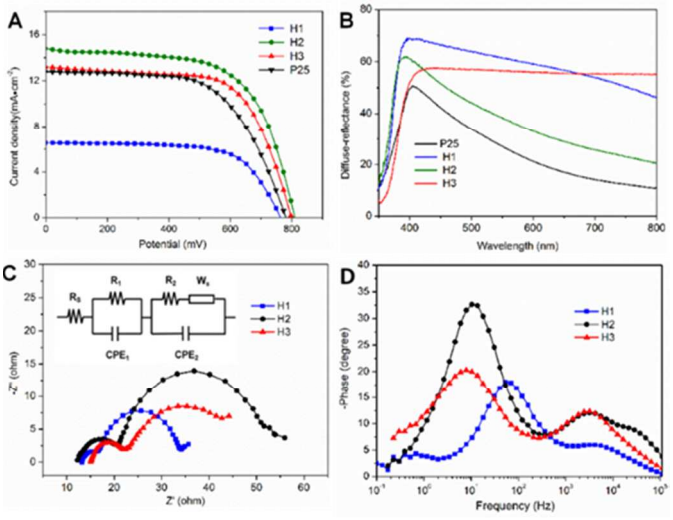

Figure 4. (A) *J–V* curves of DSCs with the photoanode of P25, H1, H2 and H3. (B) Diffuse reflectance spectra of the films based on H1, H2 and H3. (C) Niquist plots and (D) Bode plots of DSCs based on H1, H2 and H3 photoanodes measured at V_{oc} applied bias in dark.

resistance of FTO glass substrate, contact resistance, counter electrode material and the resistance of external circuits, etc. Although the substrate is identical, there is obvious difference of R_s between the three samples. The tight adhesion between the H2 photoanode and the FTO substrate derived from the reduction of crystal size should be responsible for their lower R_s. The semicircle in the high frequency region (R_1) corresponds to the interfacial resistance of the Pt/FTO substrate and redox reaction of I^-/I_3^- at the values related to the identical FTO substrate, Pt counter electrode and external circuits. The semicircle in the intermediate frequency semicircle (R_2) represents the electron transfer at the TiO_2/dye/electrolyte interface the Warburg diffusion process of I^-/I_3^- in the electrolyte at low frequency (R_{diff}). According to the approach of Adachi et al., the charge transfer (recombination) resistance (R2) related to electron-hole recombination can be determined from the central arc diameter deduced from the Nyquist plot.[26] Herein, the values of R_2 varying in the consequence of H2 (27.16 Ω) > H3 (15.71 Ω) > H1 (15.77 Ω) implying the high recombination resistance of H2 sample. As a result, this may lead to higher electron diffusion and collection efficiency in the mesoporous films.[27]

Under open-circuit voltage, there is no current passing through the external circuit, electrons injected into the TiO_2 nanocrystals would trap and detrap between conduction band and trap states and be recombined by I_3^-.[24] Therefore, the lifetime of electrons in the oxide film (τ_r) can be estimated from the maximum angular frequency (ω_{max}) of the impedance semi-circle arc at middle frequencies in the Bode spectrum. This relation can be described as $\tau_r=1/\omega_{max}= 1/2\pi f_{max}$, where f_{max} is the maximum frequency of the midfrequency peak.[26] As shown in figure 4D, the H1 photoanode shows largest ω_{max} of 53.56 Hz while the H2 and H3 presents comparable ω_{max} of 10.39 Hz and 9.11 Hz, implying longer electron lifetime as well as lower recombination rate of H2 and H3 photoanodes which can be explained by the appropriate size and surface area of these samples.[20] It is well known that charge transfer in porous nanocrystalline metal oxide electrodes follows "random walk" model that is dominated by the diffusion of carriers which can be trapped or released from trapping sites.[28] The conventional photoanodes generally composed of nanoparticles which lead to a large amount of grain boundaries as the trapping sites which retard the electron diffusion greatly as shown in Figure S5. In contrast, single-crystal-like TiO_2 crystals can provide an internal direct path way over hundreds of nanometres for electrons which can pass through the whole large crystals with reduced grain boundaries. Moreover, the nanopores in the crystals would give large surface area which can further result in enough uptake of the crystals. It is also noteworthy that the regulation of the pores and the singe-crystal-like crystals also play an important role in determining the dye loading and electron diffusion path way in DSCs.

Conclusions

In summary, a series of mesoporous anatase TiO_2 crystals were prepared with formic acid, acetic acid, octoic acid or oleic acid as solvents by a modified hydrothermal method, respectively. The integral shape of the TiO_2 crystals evolved from octahedrons to spindles and finally to spheres with different pore structures. We found that the chain length of carboxylic acids plays the pivotal role in the nucleation, growth and assembling process of the crystals which further governs the crystal size, shape, pore structure and even crystallinity. Further application of the samples as the nanoporous TiO_2 electrodes of DSCs shows a J_{sc} of 14.7 mA·cm^{-2}, a V_{oc} of 810 mV and an *FF* of 0.64, reaching a η of 7.55%. The single-crystal-like mesoporous TiO_2 crystals could avoid the high defect levels of the necking particles and provide path ways for electrons transfer directly. The submicronmeter-sized crystals could also act as light scattering centers with high light-harvesting capacity. We anticipate that such a judicious synthetic strategy to tune pore structures and integral morphologies of single-crystal-like TiO_2 crystals and further select appropriate porous crystals will open new perspectives for designing photovoltaic devices including dye-sensitized solar cells and perovskite-based hybrid solid-state solar cells.

Acknowledgements

This work was financially supported by National Natural Science Foundation of China (21373083, 21203061), SRF for ROCS, SEM, SRFDP, Programme for Professor of Special Appointment (Eastern Scholar) at Shanghai Institutions of Higher Learning, Shanghai Municipal Natural Science Foundation (12ZR1407500), Fundamental Research Funds for the Central Universities (WD1313009, WM1314018, WD1214036), and China Postdoctoral Science Foundation (2012M511056, 2013T60425).

Notes and references

[a] Key Laboratory for Ultrafine Materials of Ministry of Education School of Materials Science and Engineering East China University of Science and Technology, 130 Meilong Road, Shanghai, 200237 (China)
E-mail: hgyang@ecust.edu.cn
[b] Centre for Clean Environment and Energy, Gold Coast Campus Griffith University, Queensland, 4222, (Australia)

† Electronic Supplementary Information (ESI) available: SEM, TEM images and UV-*vis* spectra of samples. See DOI: 10.1039/b000000x/

† These authors contributed equally to this work

1 E. J. W. Crossland, N. Noel, V. Sivaram, T. Leijtens, J. A. Alexander Webber and H. J. Snaith, *Nature*, 2013, **495**, 215-219.
2 X. Feng, K. Zhu, A. J. Frank, C. A. Grimes and T. E. Mallouk, *Angew. Chem.*, 2012.
3 Y. Qiu, W. Chen and S. Yang, *Angew. Chem. Int. Ed.*, 2010, **49**, 3675-3679.
4 X. Chen, L. Liu, P. Y. Yu and S. S. Mao, *Science*, 2011, **331**, 746.

5 D. Wang, J. Liu, Q. Huo, Z. Nie, W. Lu, R. E. Williford and Y. B. Jiang, *J. Am. Chem. Soc.*, 2006, **128**, 13670-13671.
6 H. G. Yang, C. H. Sun, S. Z. Qiao, J. Zou, G. Liu, S. C. Smith, H. M. Cheng and G. Q. Lu, *Nature*, 2008, **453**, 638-641.
7 J. Pan, G. Liu, G. Q. Lu and H.-M. Cheng, *Angew. Chem.*, 2011, **123**, 2181-2185.
8 Y. Ren, Z. Liu, F. Pourpoint, A. R. Armstrong, C. P. Grey and P. G. Bruce, *Angew. Chem.*, 2012, **124**, 2206-2209.
9 J. S. Chen, D. Luan, C. M. Li, F. Y. C. Boey, S. Qiao and X. W. Lou, *Chem. Commun.*, 2010, **46**, 8252-8254.
10 J. S. Chen, Y. L. Tan, C. M. Li, Y. L. Cheah, D. Luan, S. Madhavi, F. Y. C. Boey, L. A. Archer and X. W. Lou, *J. Am. Chem. Soc.*, 2010, **132**, 6124-6130.
11 X. Chen and S. S. Mao, *Chem. Rev.*, 2007, **38**, 2891-2959.
12 B. O'regan and M. Gratzel, *Nature*, 1991, **353**, 737-740.
13 S. Yang, Y. Hou, B. Zhang, X. H. Yang, W. Q. Fang, H. J. Zhao and H. G. Yang, *J. Mater. Chem. A*, 2013, **1**, 1374-1379.
14 H. Yang, W. Fang, X. Yang, H. Zhu, Z. Li, H. Zhao and X. Yao, *J. Mater. Chem.*, 2012.
15 S. Ito, T. N. Murakami, P. Comte, P. Liska, C. Grätzel, M. K. Nazeeruddin and M. Grätzel, *Thin Solid Films*, 2008, **516**, 4613-4619.
16 A. Sanchez-Diaz, E. Martinez-Ferrero and E. Palomares, *J. Mater. Chem.*, 2009, **19**, 5381-5387.
17 C.-T. Dinh, T.-D. Nguyen, F. Kleitz and T.-O. Do, *ACS Nano*, 2009, **3**, 3737-3743.
18 J. Ye, W. Liu, J. Cai, S. Chen, X. Zhao, H. Zhou and L. Qi, *J. Am. Chem. Soc.*, 2010, **133**, 933-940.
19 S. H. Kang, S. H. Choi, M. S. Kang, J. Y. Kim, H. S. Kim, T. Hyeon and Y. E. Sung, *Adv. Mater.*, 2008, **20**, 54-58.
20 Y. Bai, H. Yu, Z. Li, R. Amal, G. Q. Lu and L. Wang, *Adv. Mater.*, 2012, **24**, 5850-5856.
21 Q. Wang, J. E. Moser and M. Grätzel, *J. Phys. Chem. B*, 2005, **109**, 14945-14953.
22 J.-C. Lin, C.-P. Lee and K.-C. Ho, *J. Mater. Chem.*, 2012, **22**, 1270-1273.
23 Y. Liu, J. R. Jennings, Y. Huang, Q. Wang, S. M. Zakeeruddin and M. Grätzel, *J. Phys. Chem. C*, 2011, **115**, 18847-18855.
24 K.-M. Lee, V. Suryanarayanan and K.-C. Ho, *Sol. Energ. Mat. Sol. C*, 2007, **91**, 1416-1420.
25 Z. He, H. Phan, J. Liu, T.-Q. Nguyen and T. T. Y. Tan, *Adv. Mater.*, 2013, **25**, 6900-6904.
26 M. Adachi, M. Sakamoto, J. Jiu, Y. Ogata and S. Isoda, *J. Phys. Chem. B*, 2006, **110**, 13872-13880.
27 D. K.-P. Wong, C.-H. Ku, Y.-R. Chen, G.-R. Chen and J.-J. Wu, *Chemphyschem*, 2009, **10**, 2698-2702.
28 S. Yang, Y. Hou, J. Xing, B. Zhang, F. Tian, X. H. Yang and H. G. Yang, *Chem.-Eur. J.*, 2013, **19**, 9366–9370.

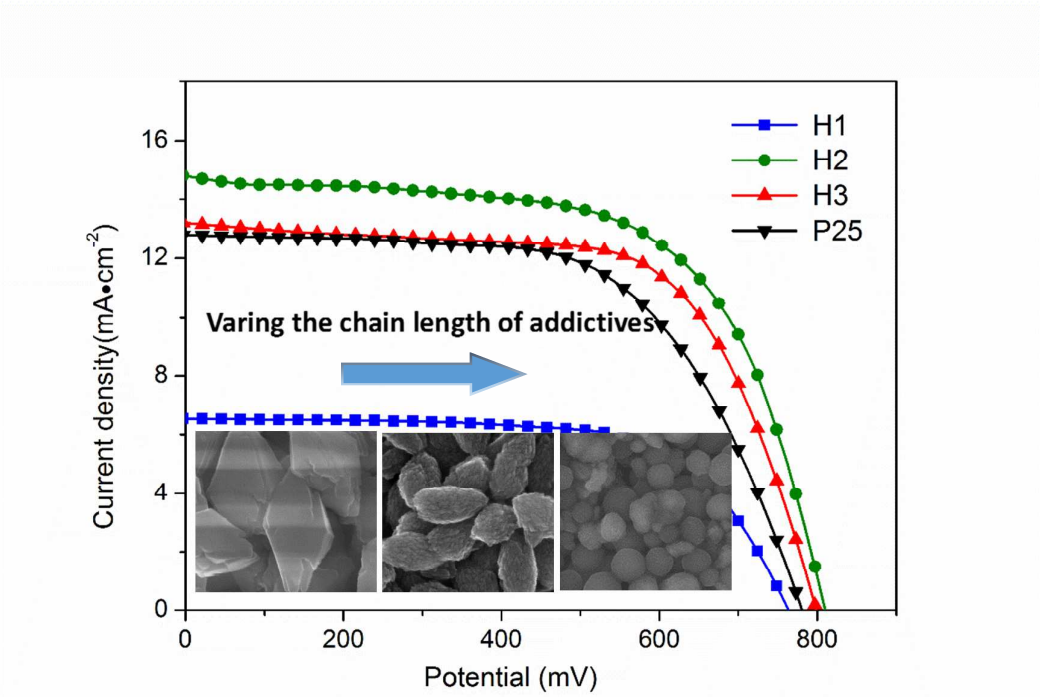

A serious of mesoporous anatase TiO_2 crystals were prepared through a hydrothermal method. By using different carboxylic acids as solvents and additives, the morphology of the integral crystals as well as inner pores can be tuned by the chain length of the carboxylic acids. Further application of these anatase TiO_2 crystals as the photoanode of DSCs attained an overall energy conversion efficiency of 7.55% due to their low electrical resistive and improved light harvesting abilities.